Int J CARS (2012) 7:687–704
DOI 10.1007/s11548-012-0768-4

ORIGINAL ARTICLE

A multi-modal approach to computer-assisted deep brain stimulation trajectory planning

Silvain Bériault · Fahd Al Subaie · D. Louis Collins · Abbas F. Sadikot · G. Bruce Pike

Received: 2 February 2012 / Accepted: 29 May 2012 / Published online: 21 June 2012

Abstract

Purpose Both frame-based and frameless approaches to deep brain stimulation (DBS) require planning of insertion trajectories that mitigate hemorrhagic risk and loss of neurological function. Currently, this is done by manual inspection of multiple potential electrode trajectories on MR-imaging data. We propose and validate a method for computer-assisted DBS trajectory planning.

Method Our framework integrates multi-modal MRI analysis (T1w, SWI, TOF-MRA) to compute suitable DBS trajectories that optimize the avoidance of specific critical brain structures. A cylinder model is used to process each trajectory and to evaluate complex surgical constraints described via a combination of binary and fuzzy segmented datasets. The framework automatically aggregates the multiple constraints into a unique ranking of recommended low-risk trajectories. Candidate trajectories are represented as a few well-defined cortical entry patches of best-ranked trajectories and presented to the neurosurgeon for final trajectory selection.

Results The proposed algorithm permits a search space containing over 8,000 possible trajectories to be processed in less than 20 s. A retrospective analysis on 14 DBS cases of patients with severe Parkinson's disease reveals that our framework can improve the simultaneous optimization of many pre-formulated surgical constraints. Furthermore, all automatically computed trajectories were evaluated by two neurosurgeons, were judged suitable for surgery and, in many cases, were judged preferable or equivalent to the manually planned trajectories used during the operation.

Conclusions This work provides neurosurgeons with an intuitive and flexible decision-support system that allows objective and patient-specific optimization of DBS lead trajectories, which should improve insertion safety and reduce surgical time.

Keywords Deep brain stimulation · Preoperative planning · Parkinson's disease · Image-guided neurosurgery · Decision-support system

Introduction

Deep brain stimulation (DBS) is an increasingly important treatment for many pharmaceutically resistant movement and affective disorders [1]. The procedure is particularly effective for moderate and severe Parkinson's disease (PD), a neurodegenerative disorder that affects 1 % of population over 60 years of age [2] and over one million people in North America [3]. DBS surgery involves the implantation of stimulating electrodes in deep brain structures (e.g., the basal ganglia or thalamus) via minimally invasive image-guided neurosurgery (IGNS) that relies on preoperative imaging of the patient's brain and precise intraoperative registration of these images with the position of the surgical tool (patient-to-image registration). Depending on the nature of the symptoms and signs, the electrodes are targeted at different nuclei of the brain. For example, the subthalamic nuclei (STN) are a common target for alleviation of motor fluctuations, dyskinesias, rigidity, tremor and slowness of movement symptoms that characterize advanced PD [3]. For essential tremor, the STN [4] and the ventral intermediate nucleus (VIM) of the thalamus [5] can both be used as target.

DBS insertion comprises multiple stages. (1) A frame-based or frameless stereotactic MRI is performed, often with injection of contrast medium, to obtain high-resolution datasets of the patient's brain. The neurosurgeon examines these images to determine precise electrode target locations

S. Bériault (✉) · F. A. Subaie · D. L. Collins · A. F. Sadikot · G. B. Pike
McConnell Brain Imaging Centre, Montreal Neurological Institute, 3801 University Street, Montreal, QC H3A 2B4, Canada
e-mail: silvain.beriault@mail.mcgill.ca

(unilateral or bilateral) and safe linear trajectories from the surface of the head to the identified targets that avoid critical brain structures, to minimize the likelihood of surgical complications. (2) In our center, the preoperative MRIs are registered to the patient during surgery, allowing tracking of the position of surgical tools. The procedure is also assisted by integration of a stereotactic atlas of the basal ganglia and thalamus [6,7]. (3) An array of 1–5 microelectrodes (2 mm apart) is then inserted, via a small burr hole and progressively advanced to the target for micro-electrode recording (MER) of neuronal activity, allowing localization of the physiological extent of the subthalamic nucleus and neighboring nuclei [8,9]. Micro- and macrostimulations are also performed, to determine salutary and untoward effects of stimulation. These measurements are complementary, and the choice of final lead placement depends on the electrode with the best MER profile and the least side-effects. (4) The deep brain stimulation electrode is then inserted, and an intraoperative CT scan (O-arm) is performed with fusion to the preoperative MRI scan to confirm adequate lead placement. (5) An MRI scan is performed after surgery to confirm electrode placement. (6) Finally, the lead is connected via an extension to a pulse generator placed in a subclavicular subcutaneous pocket under general anesthesia. (7) The deep brain stimulator is programmed over several weeks in order to achieve optimal therapeutic effect.

While intraoperative patient-to-image registration is now widely available on commercial neuronavigation platforms, the manual task of preoperative planning can be complex, time-consuming and user dependent. Despite the careful planning, significant surgery-related complications such as intra-cerebral hemorrhage, subdural hematoma, venous infarction, seizure, CSF leak, perioperative confusion and improper lead placement, have been reported [3]. Surgical complications related to electrode trajectories may be reduced by using plans designed to avoid surface veins, arteries running within sulci, ventricles, critical motor and sensory cortices, and deep nuclei such as the caudate nucleus.

The most common clinical protocol for trajectory planning involves manual inspection of a single anatomical MRI dataset: a T1w anatomical scan with gadolinium contrast (T1w-Gd [T1w-Gadolinium]) for visualization of the brain and major blood vessels. Using standard visualization tools on a commercial neuronavigation platform, the surgeon empirically searches for a safe trajectory that avoids the aforementioned critical structures. Unfortunately, with manual planning, only a few trajectories can be thoroughly analyzed in a reasonable amount of time therefore yielding subjective and potentially sub-optimal planning. Furthermore, this planning process must be systematically reproduced for each DBS case because, as shown in Fig. 1, there are sizeable variations in the choice of insertion strategies across different patients. In our center, this trajectory planning process typically takes between 10 and 25 min per target depending on the patient-specific complexity of gyral patterns, cortical atrophy and ventricular size. Another related work [10] reports planning times of up to 1 h 30 min where half the time is dedicated to choosing a suitable trajectory direction.

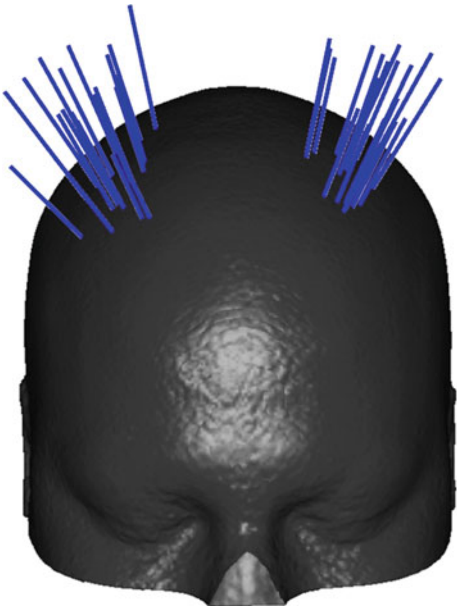

Fig. 1 Atlas of manually planned trajectories (to the left and right STN) obtained from 20 recent DBS cases performed from 2009 to 2011. This example demonstrates the significant variability with respect to the choice of DBS trajectory for a unique target. These manually planned trajectories are designed to enter at the crest of gyri and to avoid surface veins, sulci and the ventricles. Most chosen trajectories enter the brain through the second frontal gyrus

Several computer-assisted tools have been developed to help neurosurgical teams with different aspects of the overall DBS procedure, and advanced MRI techniques have been developed for direct visualization of the STN and other basal ganglia structures [11,12]. Probabilistic functional atlases relating target sites to clinical outcome have also been used for semi-automatic or automatic target prediction [13,14]. Additionally, finite element models (FEM) of the extracellular electric field were proposed to predict the volume of tissue activated [15,16]. For the specific issue of minimizing risks of complications related to electrode insertion trajectories, some experimental software platforms [17,18] have been proposed to simulate the surgical insertion and to automatically highlight any intersected critical structures along the chosen trajectory. On these platforms, the entry point selection remains empirical. Nowinski et al. [19,20] developed a high-resolution stereotactic atlas of human brain vasculature based on multiple scans of a single normal subject on 3 T and 7 T MR scanners. Recently, Navkar et al. [21] proposed an interesting volume visualization technique where the critical structures are projected onto a 3D reconstruction of the patient's skin. This visualization technique allows immediate identification of collision-free paths without the need to traverse the entire patient dataset (slice-by-slice) for each trajectory. However, arterial blood, extracted from a time-of-flight (TOF) [22] MRI dataset, is the only critical structure considered. D'Haese et al. [23] introduced the CranialVault platform to assist the surgeon throughout all stages of a DBS intervention. During preoperative planning, this platform can be used to predict suitable DBS target points [13] but the level of automation of trajectory planning is limited to a predefined (fixed) approach angle, without taking into account any patient-specific critical brain structures.

Recently, there has been considerable interest in developing computer-assisted solutions to preoperative trajectory planning for DBS and other neurosurgical procedures. These methods propose to automatically traverse and score a large number of trajectories according to a set of surgical constraints designed to mimic the decision-making process of neurosurgeons. With this new paradigm come, a number of important challenges and proposed solutions generally vary according to the choice of surgical constraints, their representation (atlas or patient based) and their aggregation.

Some methods use an anatomical atlas [24,25], aligned to the patient data, to represent the critical structures or even multi-modal atlases [26] to also include vascular and functional information. While the use of atlases yields highly customizable solutions that avoids the challenges inherent to segmentation of the critical structures on each patient dataset, most recent methods favor the latter approach because it better accounts for inter-subject variability. Segmented critical structures typically consist of the ventricles and sulci [10, 14], and some methods [27–29] also integrate patient-specific vascular information, to account for subcortical blood vessels and surface veins that do not follow gyral patterns. However, the analysis is often limited to major vessels only.

In most aforementioned methods, simultaneous avoidance of the critical structures is achieved by computation of a risk volume that weights the cost of crossing any given voxel within a patient's MRI dataset. The cost of crossing a voxel is derived from the calculation of distance maps [30], which encode the minimal distance to binary masks associated with the brain structures to avoid. Trajectories are typically ranked according to either the sum of voxel costs (e.g., in [24,26]) or according to the maximal voxel cost along the trajectory (e.g., in [28]) because almost hitting a critical structure once is more severe than approaching the same critical structure multiple times at a safer distance. Shamir et al. [29] proposed to compute both measures, to distinguish between trajectories that approach a critical structure once or many times along the path, but do not provide any ways of aggregating their two distinct rankings. Specific to DBS, Brunenberg et al. [28] also limits the search to a trajectory anterior to primary motor cortex. Alternately, Essert et al. [10] define geometric constraints to minimize the path length and to optimize the lead orientation along the target's major axis.

We present a DBS planning framework that incorporates several key innovations at every stage of the surgery planning process: from MRI acquisition to automatic trajectory selection. First, the trajectory planning is performed using a multi-modal MRI acquisition protocol that enables avoidance of several brain structures, especially venous and arterial vessels using dense susceptibility-weighted imaging (SWI) [31,32] and TOF MRI [22] datasets. Second, each trajectory is modeled as a volumetric cylinder, rather than a straight line, which easily enables the integration of complex rules that can be applied to both binary and fuzzy datasets. Third, our framework meaningfully aggregates the many constraints into a unique trajectory ranking. Automatic trajectory planning can be executed by the surgeons and the returned trajectories visualized on our interactive software platform. A retrospective analysis on a series of DBS cases is performed to validate our technique.

Methods

Overview

The flowchart of Fig. 2 shows a high-level view of the proposed framework. Two categories of user inputs must be provided to the framework: surgeon-defined inputs and MRI dataset inputs. The *surgeon-defined inputs* consist of a target point and a set of surgical constraints to optimize. The target typically depends on the symptoms to alleviate and is chosen by the neurosurgeon, from manual inspection of the MRI datasets, as part of their established clinical routine. The constraints to optimize were defined by the surgeons and are listed in section "Surgical constraints definition". The *MRI dataset inputs* are acquired via a multi-modal acquisition protocol presented in section "MRI acquisition". These raw datasets are post-processed to extract a list of entry points (i.e., the trajectories) to evaluate and to segment critical brain structures. These post-processing steps are described in section "Image processing". Finally, the surgical constraints, the segmented datasets, the target and the list of entry points are passed to our automatic trajectory planning algorithm (presented in section "Automatic trajectory planning") that meaningfully ranks the possible trajectories. Low-risk (recommended) trajectories can be further inspected by the surgeon on a convenient graphical user interface (presented in section "DBS planning framework").

Surgical constraints definition

Our automatic trajectory planning framework is governed by a set of customizable surgical constraints. Similar to the

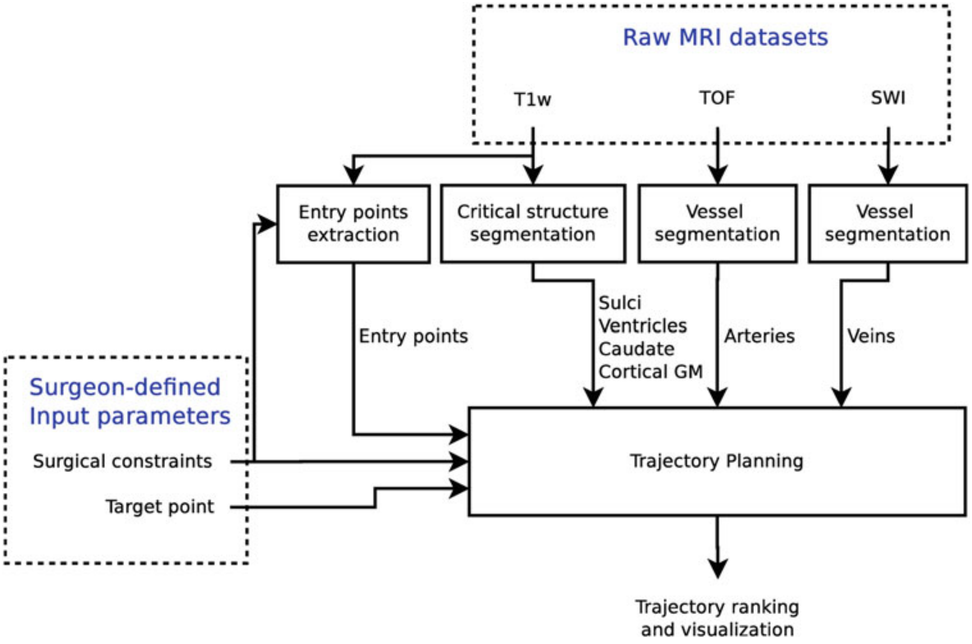

Fig. 2 High-level flowchart for multi-modal automatic trajectory planning framework

work of Essert et al. [10], our constraints are subdivided into two categories: hard constraints and soft constraints. *Hard constraints* must be satisfied and are used to discard any trajectory that intersects a critical structure or comes within an unsafe distance. *Soft constraints* are simultaneously optimized as part of our automatic trajectory planning algorithm. A core set of constraints were originally obtained from multiple interview sessions with DBS experienced neurosurgeons (see constraints #1–5 below). Experimentally, new constraints were found to interplay with the surgeon's decision-making process [33] and were introduced to the global framework (see constraints #6 and #7 below). The constraints are summarized as follows:

1. *Entry point within the frontal lobe (hard constraint)*. To reduce the risk of introducing new neurological deficits, the neurosurgeon typically selects an entry point within the frontal lobe and anterior to the primary motor cortex. Hence, our implementation concentrates the trajectory analysis within a specific cortical area of the frontal lobe (about 5 cm thick), based on the possible range of DBS trajectories exhibited in Fig. 1.
2. *Avoid the midline (hard constraint)*. The midline is avoided since it encompasses the thick mid-sagittal sinus and because the targets are off the midline. In our implementation, this hard constraint discards any entry points that are contralateral to the target.
3. *Avoid ventricles (hard/soft constraint)*. Ventricles are avoided to prevent CSF leaks, brain shifts and lead deviations [34]. A hard component is defined to eliminate any trajectory that intersects a ventricle or passes it at an unsafe distance (e.g., <2 mm). Furthermore, a soft component is defined to maximize the distance between the trajectory and the ventricles.
4. *Avoid sulci (hard/soft constraint)*. Sulci are avoided because they contain small vessels that may not be well depicted by MRI protocols. These vessels should be avoided to prevent hemorrhages [35]. A hard component is defined to eliminate any trajectory that enters a sulcus. A soft component is defined to maximize the distance between the trajectory and the sulci.
5. *Avoid subcortical blood vessels (soft constraint)*. In clinical settings, only large veins and arteries that are visible with gadolinium contrast are considered during preoperative planning. Our implementation proposes the use of advanced SWI and TOF MRI acquisition techniques. Avoidance of blood vessels is achieved with the definition of a soft constraint, applied to a fuzzy vessel segmentation dataset, to prioritize the avoidance of larger sized vessels over smaller ones.
6. *Minimize overlap with caudate (soft constraint)*. Minimizing the overlap with the caudate nucleus [8] is preferred because it is linked to symptoms of perioperative confusion. A soft constraint is therefore defined to measure the amount of voxel overlap with the caudate.
7. *Minimize overlap with cortical gray matter (soft constraint)*. Experimentally, it was found that the sulci avoidance rule alone does not prevent trajectories from intersecting the bottom of sulci (due to partial volume effects) or with large stretches of cortical gray matter

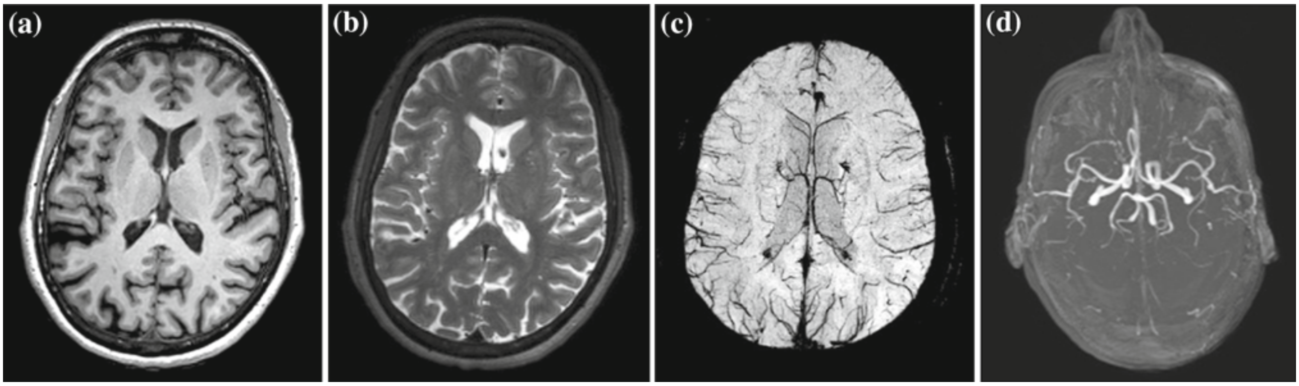

Fig. 3 Multi-modal MRI acquisition protocol. **a** T1w, **b** T2w, **c** SWI, **d** TOF

next to a sulcus, which may increase the risk of causing new neurological deficits. This soft constraint complements #3 and attempts to minimize the amount of voxel overlap with cortical gray matter.

MRI acquisition

Our MRI acquisition protocol is performed on a 3 T Siemens TIM Trio with a 32-channel head coil (see Fig. 3). First, a sagittal T1w anatomical scan of the entire head with 1 × 1 × 1-mm resolution is obtained using a 3D magnetization-prepared rapid gradient echo (MP-RAGE) sequence (TR = 2,300 ms, TI = 900 ms, TE = 2.98 ms, $\alpha = 9°$). A transverse T2w scan of the brain with 1 × 1 × 1-mm resolution is then obtained using a 3D turbo spin-echo sequence (TR = 3,200 ms, TE = 493 ms, variable flip angle). Next, a transverse SWI dataset of the brain with 0.5 × 0.5 × 1-mm resolution is obtained using a fully flow compensated 3D gradient echo sequence (TR = 34 ms, TE = 20 ms, $\alpha = 12°$, BW = 120 Hz/px). Finally, an MRA dataset is obtained with 1 × 1 × 1-mm resolution using a 3D multi-slab TOF (4 slabs, 44 slices/slab, transverse acquisition, TR = 22 ms, TE = 3.85 ms, $\alpha = 18°$). These datasets are all acquired in a single session and are aligned by linear registration (rigid body: 6 parameters, cost function: mutual information). The total acquisition time is 40 min.

The T1w, SWI and TOF datasets are used for computer-assisted trajectory planning purposes. The T2w dataset is only acquired to help surgeons with other planning duties such as target identification. The use of the SWI–TOF protocol has several advantages over the conventional T1w-Gd protocol. First, the SWI–TOF protocol does not require the injection of a contrast agent, which adds significant cost to each study and has some associated medical risks (primarily nephrogenic systemic fibrosis [36]). Second, the T1w-Gd protocol does not distinguish between arteries and veins as they both appear bright. Third, as shown in Fig. 3c, d, the SWI–TOF is capable of imaging sub-millimeter vessels with good contrast.

Image processing

Pre-processing of T1w dataset

The T1w dataset is first corrected for intensity non-uniformity using N3 (Nonparametric Non-uniform intensity Normalization) [37] and an histogram matching filter [38] is applied for intensity normalization. A binary brain mask is then estimated using the brain extraction tool (BET) [39] from the FSL library [40]. Finally, the processed T1w dataset is registered to the ICBM-152 atlas [41] using automated nonlinear image matching and anatomical labeling (ANIMAL) [42,43], which provides tissue classification (into GM, WM and CSF classes) via INSECT [44] and atlas-based labeling of the lobes and the basal ganglia nuclei.

Search-space definition

A list of brain entry points (3D coordinates) must be provided as input to the automatic trajectory planning algorithm. In our implementation, entry points were extracted from a binary voxel representation of the brain surface, where all entry points are equally spaced according to the resolution of the T1w dataset (1 × 1 × 1-mm resolution). We used binary morphological operators on the computed brain mask to identify voxels at the surface of the cortex, yielding a binary brain surface mask. Entry points outside a pre-defined bounding-box (within the frontal lobe) or contralateral to the target were automatically excluded compliance with constraint #1 and 2. For convenience, this bounding-box was defined once by the collaborating surgeons using the ICBM-152 atlas [41] and transformed to native space for each patient. The remaining entry points define the search space for automatic trajectory analysis.

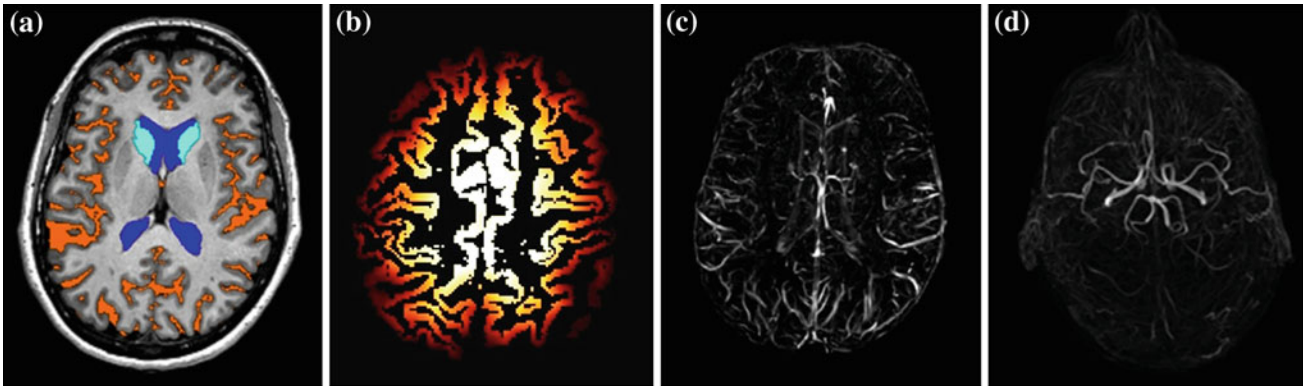

Fig. 4 The segmented critical structures. **a** Tissue classification of the T1w dataset yields binary segmentation of sulci (constraint #3), ventricles (constraint #4) and caudate (constraint #6). **b** Cortical GM voxels, obtained from tissue classification of the T1w dataset, are scaled such that a greater risk is given to GM voxels at bottom of deep sulci (constraint #7). **c**, **d** The SWI and TOF datasets are filtered for background suppression using a fuzzy vesselness measure (constraint #5)

Critical structure segmentation

Binary labels corresponding to the cerebrospinal fluid (CSF), the left and right caudate (constraint #6), and the cortical gray matter are obtained from the ANIMAL [42,43] pipeline output. The lateral ventricles (constraint #3) are segmented using a patch-based segmentation algorithm [45] and a special template of elderly subjects was used as the prior allowing more precise segmentation for patients with larger ventricles. CSF-labeled voxels inside the brain and outside the ventricles are used to define the critical sulci structures (constraint #4). Thus, all CSF voxels forming each sulcus are considered, rather than only the major sulcal lines at the surface of the cortex, since blood vessels can be located at any depth within a sulcus. Figure 4a shows an example of binary segmentation for ventricles, sulci and caudate. Cortical gray matter voxels are linearly scaled according to the minimal distance to brain surface, yielding a fuzzy dataset (see Fig. 4b for an example). Hence, a higher risk is given to cortical gray matter at the bottom of a sulcus than at the center of a gyrus (constraint #7).

Veins and arteries (constraint #5) are segmented directly from the patient's SWI and TOF datasets using a fuzzy vesselness measure [46] (see Fig. 4c, d). We chose not to apply a global threshold to the resulting vesselness datasets. Instead, the magnitude of vesselness values, at each voxel, is used to weight the relative importance of large vessels over smaller ones.

Automatic trajectory planning

The trajectory planning algorithm consists of analyzing every trajectory linking a set of brain entry points (hard constraints #1–2) to a DBS target given by the surgeon. Our algorithm is performed in two passes. A first pass quickly eliminates any trajectory that crosses through a critical structure or passes nearby at an unsafe distance (hard constraints #3–4). With the remaining trajectories, a second pass optimizes the distance to all critical structures simultaneously (soft constraints #3–7). A flowchart of the overall algorithm is shown in Fig. 5.

Trajectory modeling

Each trajectory is modeled using a cylinder of interest [33] with an N-mm radius to account for the dimension of the insertion tool, the precision of patient-to-image registration, the possible use of lateral insertion tracks (located 2 mm away from the central track) during the intraoperative MER stage and to exclude critical structures already at a safe distance (above N-mm) without any further processing. The cylinder's radius can be customized for each constraint. We used a value of $N = 5$ mm for the computation of all constraints and $N = 2$ mm for displaying the trajectories.

The mathematical model defining a trajectory cylinder is given as follows. Let S be the search space containing all the trajectories, and $\vec{t}$ a specific trajectory ($\vec{t} \in S$). Each trajectory $\vec{t}$ is a 3D line segment linking an entry point to the target. Let $\mathrm{cyl}(\vec{t})$ be the cylinder of interest centered around $\vec{t}$ and slightly extrapolated (currently, by 5 mm at both ends) to allow deeper insertions and to avoid missing veins possibly defined at the surface of the cortex. Let $d(\vec{v}, \vec{t})$ the minimal distance of any voxel $\vec{v} \in \mathrm{cyl}(\vec{t})$ from the trajectory centerline $\vec{t}$.

Surgical constraints evaluation

The trajectories are first evaluated separately for each surgical constraint. For each critical structure j, a risk value $r_j(\vec{v}, \vec{t})$ is assigned to every voxel $\vec{v} \in \mathrm{cyl}(\vec{t})$ such that:

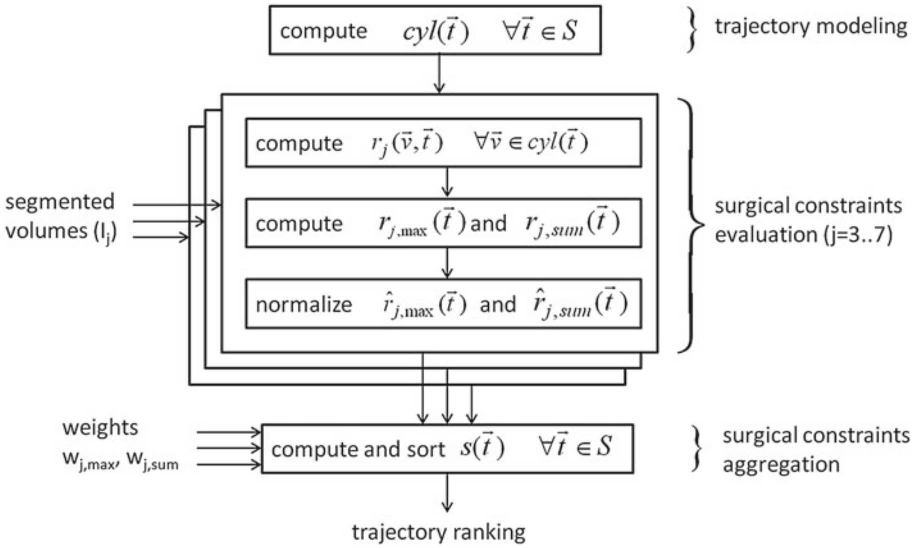

Fig. 5 Evaluation and aggregation of all soft constraints ($j = 3 \ldots 7$). For each trajectory, a cylinder of interest is projected on each segmented dataset I_j (ventricles, sulci, veins, arteries, caudate, cortical gray matter) for calculation of a voxel-wise risk (see Eq. 1). The maximal and sum of risks is then calculated (see Eq. 2) and normalized for comparison with other constraints. Finally, an aggregated trajectory score is computed according to surgeon-chosen constraints weighting

$$r_j(\vec{v},\vec{t}) = \begin{cases} I_j(\vec{v}) & d(\vec{v},\vec{t}) < k_1 \\ \frac{I_j(\vec{v})}{k_2(d(\vec{v},\vec{t})-k_1)+1} & d(\vec{v},\vec{t}) \geq k_1 \end{cases}, \tag{1}$$

where $I_j(\vec{v})$ is the value of voxel $\vec{v}$ in segmented dataset I_j. For binary datasets, $I_j(\vec{v})$ is either 0 or 1. Hence, $r_j(\vec{v},\vec{t})$ decreases monotonically with the distance $d(\vec{v},\vec{t})$ from the cylinder's centerline. For fuzzy dataset, $r_j(\vec{v},\vec{t})$ also increases monotonically with the voxel value $I_j(\vec{v})$. For example, the risk given to a particular voxel $\vec{v} \in \mathrm{cyl}(\vec{t})$ within a processed SWI or TOF dataset is computed as a combination of its distance from the trajectory's centerline ($d(\vec{v},\vec{t})$) and its vessel-likeliness value ($I_j(\vec{v})$).

The constant k_1 represents the minimal distance at which $r_j(\vec{v},\vec{t})$ starts decreasing proportionally to $d(\vec{v},\vec{t})$ and k_2 represents the speed at which $r_j(\vec{v},\vec{t})$ will decrease. We used a value of $k_2 = 1$ for all constraints. A value of $k_1 = 2$ is used for the ventricle avoidance rule (constraint #3) because any trajectory that intersects ventricles within a 2-mm radius is rejected (in the first pass of the algorithm). Similarly, a value of $k_1 = 1$ is used for the sulci avoidance rule (constraint #4). A value of $k_1 = 0$ is used for all other soft constraints (constraints #5–7).

Having computed the risk $r_j(\vec{v},\vec{t})$ for all $\vec{v} \in \mathrm{cyl}(\vec{t})$, a variety of parameters can be extracted. In this work, we compute the maximal risk and the sum of risk values:

$$\begin{aligned} r_{j,\max}(\vec{t}) &= \underbrace{\arg\max}_{\vec{v}\in\mathrm{cyl}(\vec{t})}(r_j(\vec{v},\vec{t})) \\ r_{j,sum}(\vec{t}) &= \sum_{\vec{v}\in\mathrm{cyl}(\vec{t})}(r_j(\vec{v},\vec{t})) \end{aligned} \tag{2}$$

Table 1 Weights representing each surgical constraint's relative importance were defined with the close collaboration of an expert neurosurgeon and a senior resident

Constraints	Weights	
	$w_{\max}$	w_{sum}
#3 (ventricles)	0.6	0.0
#4 (sulci)	1.0	0.0
#5a (arteries)	0.4	0.2
#5b (veins)	0.4	0.1
#6 (caudate)	0.0	0.2
#7 (cortical GM)	0.0	0.6

Surgical constraints aggregation

The $r_{j,\max}(\vec{t})$ and $r_{j,sum}(\vec{t})$ measures are then linearly normalized to a [1-100] discrete scale for comparison with other constraints [47] and are denoted $\hat{r}_{j,\max}(\vec{t})$ and $\hat{r}_{j,sum}(\vec{t})$. A final trajectory score is computed for all trajectories by aggregating the $\hat{r}_{j,\max}(\vec{t})$ and $\hat{r}_{j,sum}(\vec{t})$ parameters for all soft constraints j using a weighted cost function:

$$s(\vec{t}) = \sum_{\forall j} w_{j,\max} \cdot \hat{r}_{j,\max}(\vec{t}) + \sum_{\forall j} w_{j,\text{sum}} \cdot \hat{r}_{j,\text{sum}}(\vec{t}) \tag{3}$$

where $w_{j,\max}$ and $\mathrm{w}_{j,\text{sum}}$ are weights defined by the surgeons to represent the relative importance of each constraint j. A greater weight is typically given to the max criterion. On the other hand, the sum criterion is useful when the max criterion does not provide sufficient discrimination among the trajectories.

Suitable weights for all constraints (summarized in Table 1) were determined experimentally by the collaborating neurosurgical team, with the use of custom visualization software we developed (see next section). Although this study used the same set of weights for all subjects, the weights can easily be personalized according to the surgeon's preference or to the target type (e.g., STN DBS vs. VIM DBS). Since ventricles and sulci are typically encountered once

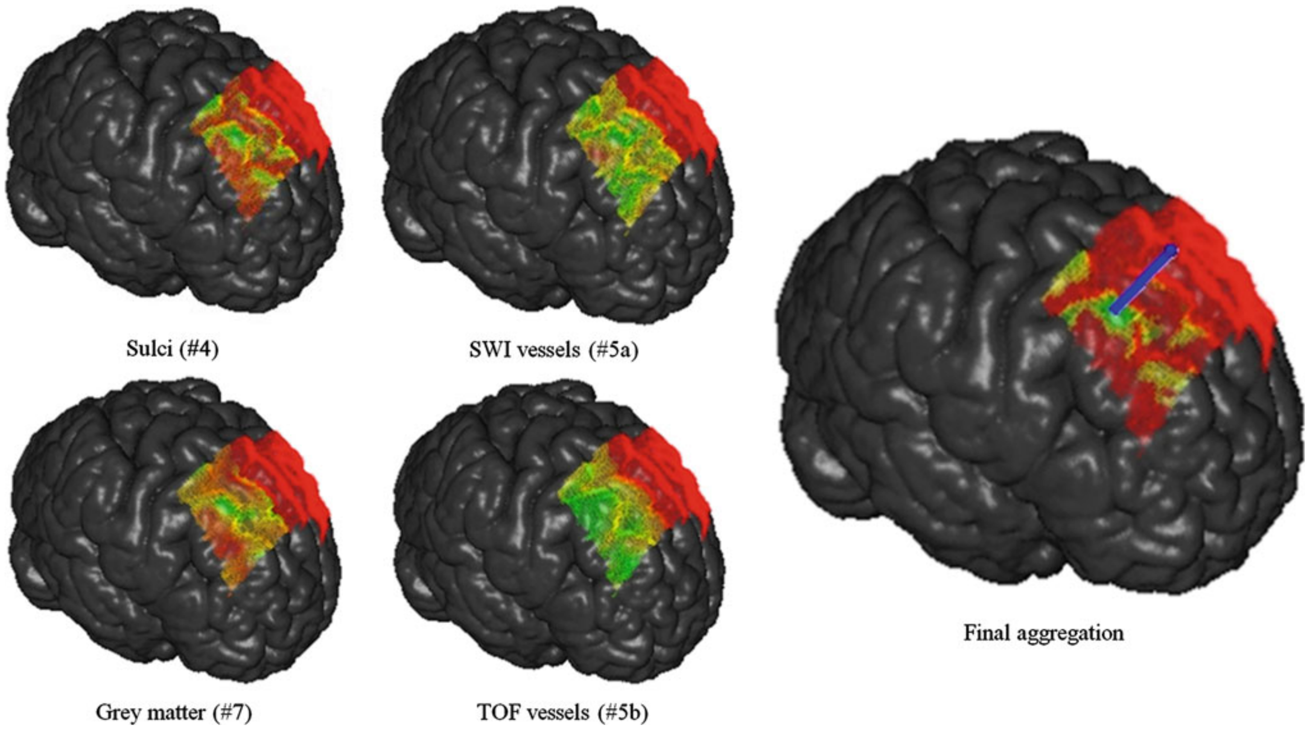

Fig. 6 Patient-specific color-coded maps of individual constraints and aggregated trajectory risk (second pass of the trajectory planning algorithm). Constraints #3 and #6 (not shown) essentially eliminates trajectories that are too medial. Constraints #4 and #7 are used to guide trajectory selection toward the center of a gyrus. Constraint #5 allows fine adjustment to the trajectory selection according to the patient-specific brain vasculature. The final aggregation map (also showing the best-ranked trajectory) provides an intuitive interface for visualization of recommended trajectories

during the course of a trajectory (near the entry for sulci and near the target for the ventricles), only the $\hat{r}_{\max}$ criterion is considered for constraints #3 and #4. Weights for constraint #5 are defined separately for veins (SWI datasets) and arteries (TOF datasets) and they include a mixture of the $\hat{r}_{\max}$ and $\hat{r}_{\text{sum}}$ criteria. For constraints #6 and #7, only the $\hat{r}_{\text{sum}}$ criterion is considered. For those specific constraints, the $\hat{r}_{\max}$ criterion does not provide sufficient discrimination of the trajectories. Indeed, most trajectories pass near the caudate and all trajectories must intersect some amount of gray matter upon entering the brain.

Clearly, vessel avoidance is a major concern during trajectory planning and consequently occupies most of the weighted cost function $s(\vec{t})$. In our work, vessel avoidance is robustly implemented via the aggregation of sulci-related constraints (constraint #4 and, to some extent, constraint #7) and the analysis of dense SWI and TOF datasets (constraint #5). Figure 6 shows an example of the computed risk before and after constraints aggregation. Constraints #4 and #7 essentially guide the trajectory selection toward the center of gyri and away from sulci (all along the trajectory) while constraint #5 allows fine trajectory adjustments based on patient-specific vascular data.

DBS planning framework

We developed an easy-to-use graphical user interface allowing surgeons to experiment with our computer-assisted trajectory planning framework. A screenshot of the application is shown in Fig. 7. Our software uses the insight segmentation and registration toolkit (ITK) [48], for the analysis of trajectories, and the visualization toolkit (VTK) [49] for 2D and 3D visualization of the trajectories.

The trajectory planning algorithm outputs an ordered ranking of low-risk (recommended) entry points, listed on the bottom-left pane of the application. These recommended entry points tend to cluster as few well-delimited patches. These patches are shown (in green) on the 3D viewing pane, which renders a color-coded map of the processed trajectories overlaid on a 3D reconstructed brain using volumetric ray casting (VTK implementation). The 2D triplanar views are used for slice-by-slice dataset visualization and allow inspection of specific trajectories, shown as a 2-mm radius cylinder projection with a customizable opacity level.

Following the automatic trajectory analysis, the surgeon can examine a few of the best-ranked trajectories sequentially. The surgeon can also coarsely position the trajectory cursor to a specific low-risk area (e.g., within a green patch)

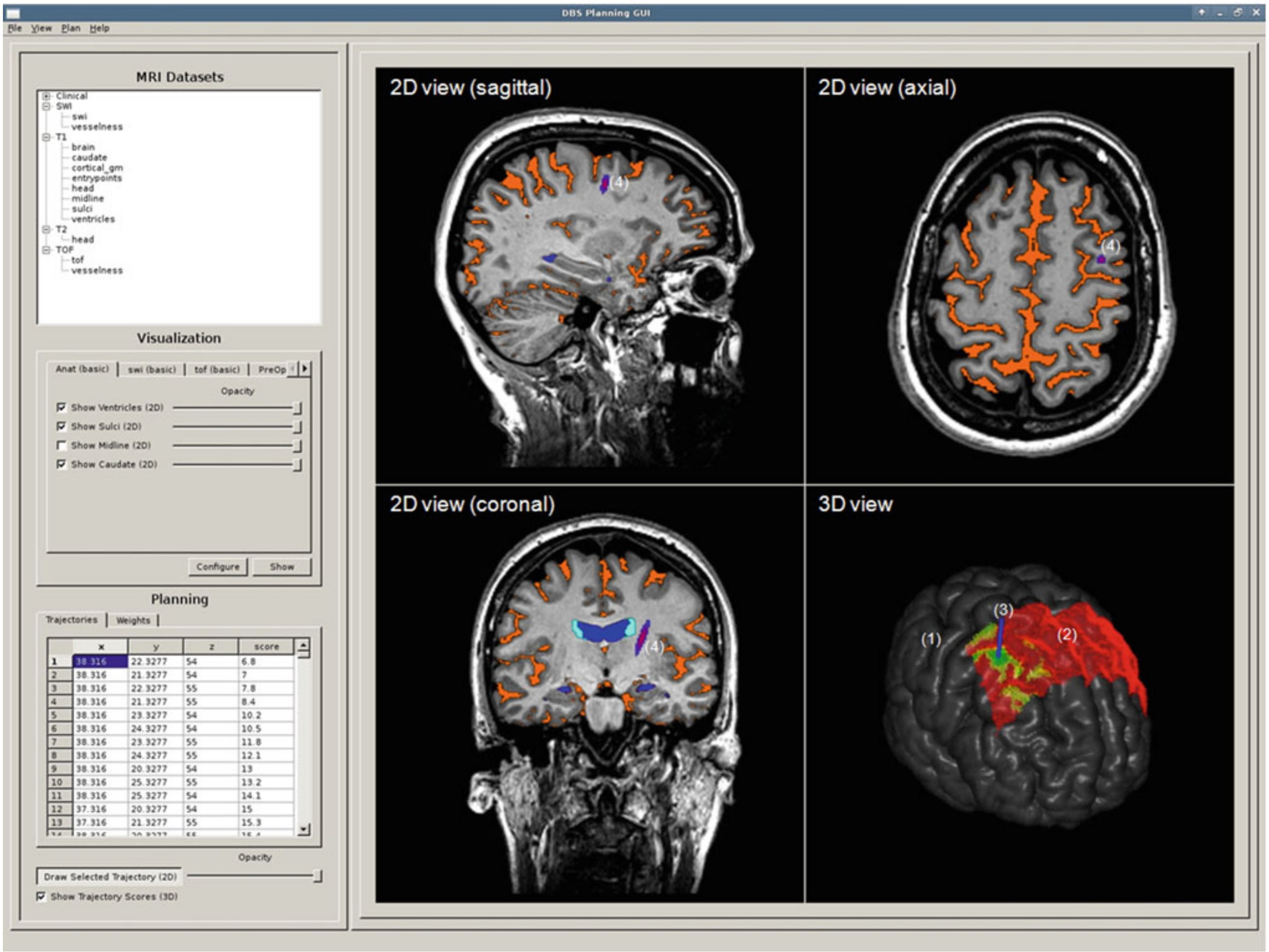

☑ Show Ventricles (2D)
☑ Show Sulci (2D)
☐ Show Midline (2D)
☑ Show Caudate (2D)

	x	y	z	score
1	38.316	22.3277	54	6.8
2	38.316	21.3277	54	7
3	38.316	22.3277	55	7.8
4	38.316	21.3277	55	8.4
5	38.316	23.3277	54	10.2
6	38.316	24.3277	54	10.5
7	38.316	23.3277	55	11.8
8	38.316	24.3277	55	12.1
9	38.316	20.3277	54	13
10	38.316	25.3277	55	13.2
11	38.316	25.3277	54	14.1
12	37.316	20.3277	54	15
13	37.316	21.3277	55	15.3

☑ Show Trajectory Scores (3D)

Fig. 7 Graphical user interface for trajectory planning and visualization. Figure annotation: (*1*) volume rendering of the brain, (*2*) color-coded map of entry points (most recommended trajectories are shown as small green patches), (*3*) interactive cursor for trajectory selection and (*4*) triplanar visualization of the selected trajectory shown as a 2- mm radius cylinder

Table 2 Breakdown and classification of major DBS planning tasks impacted by the use of the proposed framework

DBS planning task	Stage	Level of automation	Processing time
MRI acquisition	Preoperative	Manual	40 min
Image processing	Preoperative	Automatic	<2 h
Target identification	Intraopeartive	Manual	(Unchanged)
Surgical constraints evaluation	Intraoperative	Automatic	<20 s
Surgical constraints aggregation	Intraoperative	Automatic or semi-automatic	<1 s

on the interactive 3D viewing window. Our software can then automatically generate a sub-ranking of all trajectories within that patch, up to a user-defined search angle, and identify the local minima within that patch. This search tool can be used to efficiently examine recommended trajectories among different patches and to exclude specific patches due to other planning considerations not covered by the implemented constraints.

The proposed framework can be integrated with the overall surgical workflow as a decision-support system that provides neurosurgeons with value-added visual feedback during DBS planning. Table 2 summarizes the major planning tasks involved using the proposed framework. These tasks are classified according to the stage at which they occur (preoperative or intraoperative) and the level of automation (automatic, semi-automatic or manual). Preoperative tasks are less time sensitive as they are typically executed the day before the surgery. Intraoperative tasks are time sensitive as they are executed within the operating room. Tasks that require no user interaction are classified as “automatic”.

Tasks that require some user interaction for each case are classified as "semi-automatic". Tasks that are unmodified with respect to conventional clinical routines are classified as "manual".

Our framework integrates most optimally with the workflow of a frameless DBS approach where the patient can undergo preoperative MRI at least 1 day before surgery. This is due to the processing time required for image segmentation and registration. In our center, preoperative MRI acquisition is typically performed prior to the surgery without the stereotactic frame. These preoperative images are uploaded to a frameless IGNS platform (Medtronic StealthStation^{R}) used for preoperative planning. A neuronavigation technician post-processes the preoperative MRI to segment the brain cortex and surface blood vessels using image intensity thresholding and manual drawing tools offered on the IGNS platform, which are reviewed by the neurosurgeon. In this work, we substituted the use of gadolinium contrast MRI with a novel multi-modal MRI protocol, described in section "MRI acquisition". Furthermore, we developed an automatic image processing pipeline that requires no user interaction and that automates the preprocessing segmentation and registration steps described in section "Image processing".

During surgery, frameless stereotaxy based on the preoperative MRI scan is used to evaluate suitable trajectories to the target. To do so, the surgeon interactively selects the target point and manually examines a few possible trajectories on the IGNS platform using 3D, triplanar and probe's eye views. A marker is placed on the patient's head at the entrance of the chosen trajectory indicating where to perform the burr hole. Using our framework, the target identification task remains unchanged. Our graphical user interface allows interactive target identification from direct visualization of the co-registered T1w and T2w datasets. Alternately, the target coordinates can also be passed to the software if a third-party targeting method is used. The only change to the intraoperative surgical workflow consists of executing the automatic trajectory planning algorithm, which provides intuitive representation of suitable insertion areas to facilitate the final decision-making. The surgical constraints evaluation requires no user initialization and a multi-threaded implementation executes in less then 20 s for a search space of over 8,000 trajectories on a general purpose personal computer (quad core, 2.66 GHz, 4 GB RAM) running Linux. The surgical constraints aggregation executes in less then 1 s, thus allowing the surgeon to generate alternate plans, semi-automatically using different constraints weights, in a timely manner. In this study, a fixed set of weights were used for all patients.

It should be noted that our framework can also be integrated with the workflow of a frame-based DBS approach as long as preoperative imaging datasets are accessible prior to the surgery for the image preprocessing tasks. The processed datasets can then be linearly aligned within few minutes to the MRI dataset exhibiting the stereotactic frame typically acquired at the beginning of the surgery. Furthermore, the neurosurgeon remains in control of the final choice of insertion trajectory.

Experiment

Validation methodology

The goal of computer-assisted trajectory planning is twofold: to improve the efficiency of preoperative planning but, more importantly, to propose safer alternatives to the surgeon. This latter goal poses key validation challenges because, in absence of a ground truth, it is difficult to assess whether automatic methods yield superior trajectory planning, in comparison with the manual protocol. In some related works (e.g., [21,28]), trajectories are validated qualitatively, by experienced neurosurgeons, from manual inspection of the trajectories or via small questionnaires. In other studies [10,29,33], a numerical comparison is performed to show how automatically computed trajectories yield better optimization scores of the defined surgical constraints than the manual trajectories. This validation method makes a fundamental assumption that surgeons attempt to optimize the same set of surgical constraints, and only those constraints, during their manual planning protocol.

Our work is validated with a retrospective, in-depth analysis of recent DBS planning cases, with the motor part of the STN as the target because it is arguably the most prevalent target for PD patients with severe rigidity. We first ran a conventional numerical analysis to compare the risk values between our automatically planned trajectories (T_{auto}) and the actual surgical trajectories planned manually by the surgeon (T_{manual}). Then a qualitative evaluation of the trajectories returned by our framework was performed by two neurosurgeons with DBS expertise to assess whether these computed trajectories are suitable for surgery.

Patients

Eight PD patients with severe rigidity symptoms (4 males, 4 females; age, 46–67) volunteered to participate in this study after providing an informed consent. The implants were bilateral for 6 subjects and unilateral for 2 subjects, for a total of 14 planning cases. This study was approved by the research ethics committee of the Montreal Neurological Institute (MNI). Each patient underwent three separate MRI scanning sessions as follows:

1. Preoperative T1w, SWI and TOF datasets were acquired at 3 T and were linearly registered according to the MRI protocol described in section "MRI acquisition".

Table 3 Comparison between automatic and manual planning (in parenthesis) for all 14 cases. The individual scores for each soft constraint are normalized to a scale of [1–100] for comparison with other constraints

Case #	Constraint							
	#3 (ventricles)	#4 (sulci)	#5a (TOF)		#5b (SWI)		#6 (caudate)	#7 (GM)
	$\hat{r}_{\max}$	$\hat{r}_{\max}$	$\hat{r}_{\max}$	$\hat{r}_{\mathrm{sum}}$	$\hat{r}_{\max}$	$\hat{r}_{\mathrm{sum}}$	$\hat{r}_{\mathrm{sum}}$	$\hat{r}_{\mathrm{sum}}$
#1	1 (1)	2 (38)	16 (17)	3 (2)	29 (23)	47 (15)	57 (33)	14 (64)
#2	1 (1)	2 (48)	18 (52)	3 (9)	1 (2)	27 (19)	37 (17)	10 (9)
#3	1 (1)	2 (88)	10 (14)	7 (21)	24 (24)	20 (85)	1 (5)	14 (94)
#4	1 (89)	1 (71)	10 (19)	5 (18)	8 (45)	15 (57)	2 (72)	1 (55)
#5	1 (1)	1 (80)	1 (33)	1 (3)	1 (17)	6 (7)	27 (22)	5 (76)
#6	1 (1)	8 (64)	1 (43)	1 (10)	11 (19)	3 (6)	5 (14)	1 (81)
#7	1 (1)	1 (1)	1 (1)	1 (1)	6 (6)	6 (6)	2 (2)	2 (2)
#8	1 (95)	5 (18)	19 (16)	24 (18)	19 (32)	9 (10)	1 (52)	6 (52)
#9	1 (1)	1 (20)	1 (9)	1 (2)	2 (3)	12 (26)	8 (8)	6 (11)
#10	1 (–)	1 (–)	14 (–)	2 (–)	8 (–)	3 (–)	11 (–)	3 (–)
#11	1 (1)	1 (27)	27 (16)	8 (3)	8 (19)	18 (35)	6 (22)	6 (11)
#12	1 (1)	2 (9)	19 (21)	41 (32)	8 (11)	5 (4)	2 (6)	2 (13)
#13	1 (1)	8 (8)	17 (24)	10 (5)	3 (10)	21 (4)	3 (1)	5 (9)
#14	1 (1)	1 (80)	1 (1)	1 (7)	4 (14)	4 (22)	2 (21)	2 (33)
Avg.	1 (15)	3 (42)	11 (20)	8 (10)	9 (17)	14 (23)	12 (21)	6 (39)

These datasets were used for evaluating the proposed automatic trajectory planning method.

2. A preoperative T1w-Gd dataset was acquired at 1.5 T as part of the patient's regular clinical treatment. This dataset was used by the neurosurgeon to plan the DBS lead insertion after manual evaluation on triplanar, trajectory and probe's eye views provided on the Medtronic StealthStation^{R} planning platform. This dataset is linearly registered to the 3 T T1w dataset (affine: 9 parameters, cost function: cross-correlation).
3. A postoperative T1w MRI was acquired on at 1.5 T as part of the patient's regular clinical treatment. This dataset exhibits the final position of the inserted electrode and DBS lead and is linearly registered to the 3 T datasets (rigid body: 6 parameters, cost function: cross-correlation).

Identification of T_{auto} and T_{manual}

For all DBS cases, the target point coordinates were identified by an experienced neurosurgeon using the registered postoperative and pre-operative T1w datasets. These target points were passed to our automatic planning framework and best-ranked trajectories (T_{auto}) generated by our algorithm were kept for the comparison.

The coordinates of the real entry points, corresponding to the manually planned trajectories (T_{manual}), were then estimated from the postoperative MRI. However, it was challenging to obtain a precise estimate of T_{manual} while taking into account the possible registration errors and geometric distortions caused by the presence of the lead and, more importantly, errors due to postoperative electrode bending caused by the removal of the stylet and guide tubes at the end of the surgery. We estimated the lead orientation as a straight line linking two points, manually identified by the neurosurgeon, along the observed trajectory. These points were precisely chosen within the trajectory segment that remains straight post-surgery. The first point was selected at the bottom of the multi-contact electrode. The second point was selected along the trajectory and was separated by at least 3 cm to minimize extrapolation errors. We then extrapolated the trajectory to the brain surface. For the numerical comparison of section "Quantitative evaluation", we compensated for possible inaccuracies in the estimation of T_{manual} by retrieving the trajectory with the smallest aggregated risk (as computed by our planning algorithm) within a $\pm 1.0°$ range of T_{manual}. For the qualitative comparison of section "Qualitative evaluation," the collaborating neurosurgeons evaluated T_{manual} using both the reconstructed trajectory on preoperative data and the actual path taken by the electrode directly visualized on postoperative MRI. The later step safeguards against any possible errors introduced by trajectory reconstruction and image registration.

Results

Quantitative evaluation

For all 14 DBS insertions, constraint-specific risk values were extracted and a comparison of the optimization achieved with

Table 4 Minimal distance to ventricles and sulci for T_{auto} and T_{manual}

Case #	Dist. to ventricles (mm)		Dist. to sulci (mm)	
	T_{auto}	T_{manual}	T_{auto}	T_{manual}
#1	>5.0	>5.0	3.7	1.9
#2	>5.0	>5.0	4.6	1.7
#3	>5.0	>5.0	3.3	1.8
#4	>5.0	2.2	4.1	1.3
#5	>5.0	>5.0	4.0	1.2
#6	>5.0	>5.0	3.5	1.4
#7	>5.0	>5.0	4.7	4.7
#8	>5.0	2.1	3.5	2.6
#9	>5.0	>5.0	4.0	2.5
#10	>5.0	–	4.2	–
#11	>5.0	>5.0	4.5	2.4
#12	>5.0	>5.0	4.2	3.4
#13	>5.0	>5.0	3.4	3.4
#14	>5.0	>5.0	4.9	1.2
Avg.	>5.0	4.6	4.0	2.3

T_{auto} and the estimated T_{manual} is shown in Table 3. For case #7, T_{auto} falls inside the range of uncertainty of T_{manual} and therefore both trajectories are considered identical. Risk values for T_{manual} of case #10 are not available because the trajectory was posterior to the search space (defined by surgical constraint #1). Table 4 shows the minimal distance (in millimeters) to the sulci and ventricles binary structures.

Clearly, the computed trajectories generally exhibit smaller risks (a relative measure of how well a particular constraint is met in comparison with other possible trajectories) than the manual trajectories, simultaneously for each surgical constraint taken separately. Furthermore, constraints with higher weights receive more optimization and have less fluctuation in their score from one case to another. For example, constraints #3, 4 and 7 (ventricle, sulci, and cortical gray matter) always exhibit a risk inferior to 20 (out of 100) and most often inferior to 10 (out of 100).

Our automatic solution tends to return trajectories well within the middle frontal gyrus (a region of the frontal lobe that encompasses several smaller gyri commonly used for STN DBS) that optimally satisfy the ventricle avoidance rule (minimum distance >5 mm even for cases with larger ventricles) and in many cases the caudate rule as well. On the other hand, few manually planned trajectories entered the brain in more medial patches of the middle frontal gyrus region, yielding trajectories closer to the ventricles (e.g., case #4 and #8).

The minimal distance to sulci is always above 3 mm and sometimes above 4 mm for all automatic trajectories. With the integration of constraint #7, even very narrowed sulci that are sensitive to partial volume effects can be avoided. Figure 8 shows an example of an automatically planned trajectory that enters the brain at the center of a gyrus and also avoids neighboring sulci along its entire course to the STN.

Regarding the avoidance of SWI and TOF detected blood vessels, some improvements to the optimization of risk values is generally observed, especially since only major blood vessels, visible on gadolinium enhanced T1w dataset, are avoided using the manual protocol. As shown in the example of Fig. 9 (for case #4), the integration of SWI–TOF to our framework can yield automatically planned trajectories that better avoid subcortical veins with minimal impact to other constraints.

Qualitative evaluation

The previous section showed that T_{auto} generally improves the simultaneous optimization of a well-defined set of surgical constraints, but does not show whether T_{auto} fully mimics the surgeon's decision-making process and whether it is suitable for surgery. Furthermore, it does not show whether T_{auto} is truly optimal or simply over-fitted to imperfections in the raw and segmented datasets due to considerable motion sometimes visible in the PD patients' MRI data. Hence, for all 14 DBS insertions, T_{auto} and T_{manual} were qualitatively evaluated by two neurosurgeons with DBS expertise. To do so, the multi-modal 3 T MRI datasets (T1w, SWI, TOF) used for the automatic trajectory analysis, as well as the clinical preoperative (T1w-Gd) and postoperative MRI for which the surgeons are most familiar with, were uploaded to our visualization software.

Without performing a comprehensive qualitative analysis, which would have been outside the scope of this paper, the surgeons were asked to navigate, slice-by-slice, through T_{auto} and T_{manual} on the various imaging contrasts available. The surgeons first evaluated T_{auto} on the co-registered multi-modal 3 T MRI (T1w, SWI, TOF) on the co-registered clinical T1w-Gd dataset for confirmation and were asked to comment whether T_{auto} is suitable for surgery. Then, the surgeons evaluated T_{auto} and T_{manual} on those same datasets and were asked to comment whether they consider T_{auto} a preferable alternative to T_{manual}. To exclude possible inaccuracies in the estimation of T_{manual} from interfering with the comparison, the surgeons also evaluated T_{manual} directly on the postoperative MRI to confirm their assessment.

Table 5 summarizes the surgeons' analysis for each case. All 14 cases automatically planned by our software were judged suitable for surgery. In 5 cases (case #2, 4, 8, 10, 14), T_{auto} was judged a significant improvement over T_{manual} by both neurosurgeons. In 8 other cases, (case #1, 5–7, 9, 11–13) T_{auto} was judged equivalent or preferable to T_{manual}.

For case #3, both surgeons expressed a slight preference for T_{manual} even though T_{auto} was judged suitable and seemed to improve the optimization of the sulci constraints. For this

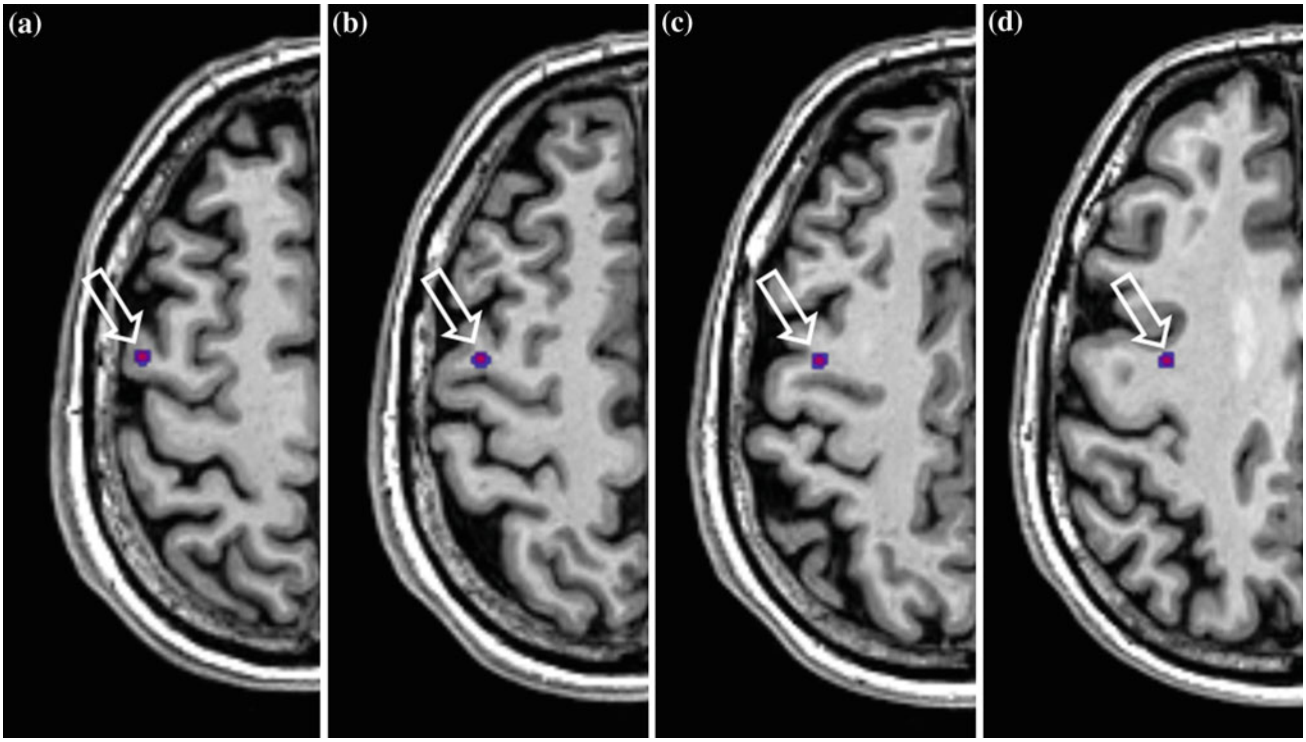

Fig. 8 Few transverse slices of the automatic trajectory (T_{auto}) for case #4. The intersection of the probe path with the transverse slice is shown as a *small purple dot* (*arrow*). This example shows how the combination of constraints #3 and #7 yields a trajectory that stays at a safe distance from the sulci along the entire path

specific case, a concern was raised because T_{auto} was posterior to T_{manual}, although still within the pre-motor cortex (middle frontal gyrus) and anterior to T_{manual} of another case (case #10). This observation suggests that surgeons prefer more anterior entry points whenever allowed by other constraints.

For case #12, T_{auto} was judged suitable but one surgeon expressed a minor concern regarding its proximity to a surface vein visualized well on the clinical T1w-Gd dataset. As opposed to arteries, surface veins do not follow the sulcal patterns and must be adequately planned for to prevent risk of venous infarction. In our framework, veins are primarily imaged using the SWI acquisition yielding dark blood. Automatic segmentation of dark surface veins is somewhat challenging since CSF surrounding the cortex is also dark. Consequently, surface veins do not entirely match the tubular structure assumption posed by the use of conventional vesselness filter [46] and therefore admit lower vessel-likeliness values in comparison with subcortical veins. However, this limitation did not seem to affect the global quality of T_{auto} for the 14 cases presented in this work.

For case #5, our software detected that T_{manual} was almost intersecting a sulcus (see Table 4). However, this observation is less obvious when visualizing T_{manual} on the postoperative MRI. Indeed, because a rigid-body transformation was used to register the postoperative MRI (the only viable option due to the distortion caused by lead implant), changes in the gyral patterns, caused by postoperative brain shifts, were not always adequately aligned. This shows that, for the sulci avoidance constraint, a numerical comparison alone is

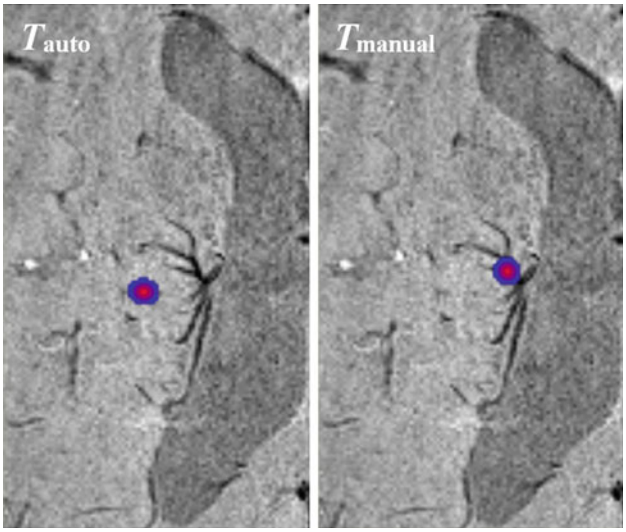

Fig. 9 Avoidance of subcortical venous blood vessel for case #4 using automatic (T_{auto}) and manual (T_{manual}) trajectory planning

Table 5 Qualitative comparison of manual (T_{manual}) and automatic (T_{auto}) trajectories by two neurosurgeons with DBS expertise (referred as S1 and S2)

Case	T_{auto} validity		Preferred trajectory		Qualitative description of T_{auto} and T_{manual}
	S1	S2	S1	S2	
#1	Yes	Yes	Eq.	T_{auto}	T_{auto} and T_{manual} are separated by an angle of 6.1° and have similar characteristics. Both trajectories avoid the ventricles, sulci and surface veins. Both trajectories have some overlap with the caudate and, in both cases, is considered a minor issue
#2	Yes	Yes	T_{auto}	T_{auto}	T_{auto} and T_{manual} are separated by an angle of 5.2°. Both trajectories avoid ventricles, caudate and surface veins. T_{auto} avoids sulci and even cortical gray matter along sulci
#3	Yes	Yes	T_{manual}	T_{manual}	T_{auto} and T_{manual} are separated by an angle of 21.6° and are entering the brain through different gyri. T_{manual} is more anterior than T_{auto}. Both trajectories avoid the ventricle and caudate. T_{manual} is closer to a sulcus
#4	Yes	Yes	T_{auto}	T_{auto}	T_{auto} and T_{manual} are separated by an angle of 15.7° and T_{manual} is more medial than T_{auto}. T_{manual} enters the caudate and the subependymal wall of the lateral ventricles. T_{auto} fits all criteria of ventricle, caudate, sulci and surface veins
#5	Yes	Yes	Eq.	Eq.	T_{auto} and T_{manual} are separated by an angle of 9.1°. T_{auto} fits all criteria of ventricle, caudate, sulci and surface veins. T_{manual} seems closer to a sulcus
#6	Yes	Yes	Eq.	T_{auto}	T_{auto} and T_{manual} are separated by an angle of 4.5° and have similar characteristics. Both trajectories avoid ventricles, caudate and surface veins. T_{auto} approaches a sulcus once at a safe distance. T_{manual} is slightly closer to that same sulcus
#7	Yes	Yes	Eq.	Eq.	T_{auto} and T_{manual} are separated by an angle of 0.9° and are considered identical since T_{auto} is inside the range of uncertainty associated with T_{manual}. Both trajectories fit all criteria of ventricle, sulci, caudate and surface vein avoidance
#8	Yes	Yes	T_{auto}	T_{auto}	T_{auto} and T_{manual} are separated by an angle of 13.9°. T_{manual} enters the subependymal gray near the lateral ventricles and abuts on a sulcus without crossing it. T_{auto} fits all criteria of ventricle, sulci, caudate and surface veins
#9	Yes	Yes	Eq.	Eq.	T_{auto} and T_{manual} are separated by an angle of 2.0° and are therefore very similar. T_{manual} enters the subependymal gray near the lateral ventricles and abuts on a sulcus without crossing it. T_{auto} fits all criteria of ventricle, sulci, caudate and surface veins perfectly
#10	Yes	Yes	T_{auto}	T_{auto}	T_{auto} and T_{manual} are separated by an angle of 16.2°. T_{manual} enters the subependymal wall, too close to the lateral ventricles, and is posterior to the search space delimited with constraint #1. T_{auto} is still slightly posterior but within the allowed search space. T_{auto} fits all criteria of ventricle, sulci, caudate and surface veins even if patient has cortical atrophy and enlarged sulci
#11	Yes	Yes	Eq.	T_{auto}	T_{auto} and T_{manual} are separated by an angle of 4.2° and share similar characteristics. T_{auto} fits all criteria of ventricles, caudate, sulci and surface vein avoidance
#12	Yes	Yes	Eq.	T_{auto}	T_{auto} and T_{manual} are separated by an angle of 3.9° and share similar characteristics. T_{auto} fits all criteria of ventricles, caudate, sulci. However, T_{auto} comes close to a surface vein (visible on the T1w-Gd dataset)
#13	Yes	Yes	Eq.	Eq.	T_{auto} and T_{manual} are separated by an angle of 27.7°. Both trajectories fit all criteria of ventricles, caudate, sulci and surface veins avoidance. T_{manual} is more posterior but it was not considered an issue
#14	Yes	Yes	T_{auto}	T_{auto}	T_{auto} and T_{manual} are separated by an angle of 5.4°. T_{auto} fits all criteria of ventricles, caudate, sulci and surface veins avoidance. T_{manual} abuts the bottom of a sulcus. T_{auto} improves avoidance of cortical gray matter along the same suclus

not sufficient and may underestimate the quality of T_{manual} for cases with significant bending of the lead.

In this study, T_{auto} was selected automatically as the trajectory with the absolute lowest score (i.e., the global minima) because our research objective was to design a DBS planning framework that necessitates the least amount of user interaction. Based on the results of Table 5, there were cases where T_{auto} and T_{manual} belong to the same patch and cases where T_{auto} and T_{manual} belong to different patches (within the middle frontal gyrus). For example, T_{auto} and T_{manual} for cases #3, 4, 8, 10, 13 are each separated by more then 15°. We could have used an alternate low-risk trajectory that is closer to T_{manual} for the comparison since, as explained in section "DBS planning framework", our software is also capable of retrieving the local minima within the neighborhood of a given trajectory (i.e., T_{manual}) but, interestingly, for 3 of these cases (cases #4, 8, 10), both surgeons retrospectively preferred our T_{auto} proposal over the surgically chosen T_{manual}.

While both the manual and automatic methods are suitable for DBS planning, the automatic method tends to qualitatively improve the simultaneous avoidance of many critical structures and allows the neurosurgeon different options that can then be evaluated in an efficient manner.

Hence, the automatic approach reduces the cognitive work to a set of recommended trajectories that are easy to navigate with our user interface.

Discussion

This work proposes a decision-support system for assisting the neurosurgeon during the preoperative planning phase of DBS neurosurgery. Our framework is capable of analyzing a large number of trajectories simultaneously against many surgical constraints defined across multi-modal imaging datasets. Trajectories are ranked according to a weighted cost function of the surgical constraints and a software application was developed to allow easy integration of computer-assisted trajectory planning within the global surgical workflow, thus providing neurosurgeons with value-added information to facilitate their decision-making. We retrospectively validated our framework on a cohort of Parkinson's patient, using the STN as the target, although the implemented constraints were generically designed and can also be applied to other DBS targets.

A retrospective comparison revealed that automatic planning tends to improve the optimization of many neurosurgeon-chosen constraints, mostly because thousands of trajectories can be analyzed in less then 20 s whereas only few trajectories can be evaluated using the manual approach in a reasonable amount of time. However, automatic methods are typically limited to the optimization of a pre-defined set of constraints, hence disregarding potentially undescribed constraints that can interplay with the surgeon's decision-making. Furthermore, trajectories are most probably optimized based on non-ideally segmented critical structure datasets. Hence, a qualitative evaluation, by two neurosurgeons with DBS expertise, was necessary to further validate the proposed trajectories. For all cases, the automatically recommended trajectory was judged suitable upon evaluation by the neurosurgeon.

Our framework made use of relatively new MRI modalities that provide dense and separate datasets for venous and arterial blood vessels visualization. The total scan time associated with this new MRI protocol is about 40 min, which may be long for elderly PD patients. Various strategies are available to reduce the additional 25 min required for SWI and TOF acquisition. First, it is possible to reduce the number of slices to only cover the volume from outside of the head to the basal ganglia. Second, it is possible to slightly increase the slice thickness of the SWI acquisition since this particular sequence benefits from anisotropic resolution for capturing veins with arbitrary orientation [50]. If no additional scan time is available for the SWI and TOF acquisitions, it remains possible to apply constraint #5 to vessel information found on a clinical T1w-Gd dataset. The multi-modal datasets were acquired within a single scanning session and were aligned using linear (rigid-body) registration. Nonlinear registration could have been used to account for geometric distortions but it was not found necessary on the overall group of patients. Furthermore, in section "Qualitative evaluation", the neurosurgeons cross-validated the computed trajectories on a co-registered clinical T1w-Gd dataset where blood vessels are imaged as part of the T1w navigation scan.

We decided to model the insertion lead as a volumetric cylinder of interest that intersects the segmented datasets directly, rather than the conventional approach of a straight line that samples a pre-calculated distance map. While the latter is computationally efficient, our model offers several advantages. First, a cylinder model is more representative of the physical lead used for the insertion and it implicitly acts as a safety buffer to account for the multiple insertions performed during the MER stage. Second, the computation of distance maps is highly sensitive to false positive voxels over large clusters representing true critical structures [33]. Third, our model can be applied efficiently on fuzzy datasets, which enables the implementation of complex rules and the integration of SWI and TOF datasets without the use of a global threshold. Fourth, this approach prevents over-fitting for one specific constraint, because the analysis is locally applied within the cylinder of interest. For example, if a trajectory is already 5- mm away from the ventricles, the optimizer should concentrate on the remaining constraints, rather than searching for a trajectory that avoids the ventricles beyond that distance. The use of a cylinder model remains fast and the trajectory analysis is usually completed in less than 20 s using the search space defined by constraint #1 and high-resolution datasets ($1 \times 1 \times 1$- mm for the T1w and TOF and $0.5 \times 0.5 \times 1$- mm resampled to $0.5 \times 0.5 \times 0.5$- mm isotropic for the SWI).

As with manual trajectory planning, our framework computes linear lead trajectories based on preoperative MRI without taking into account possible occurrence of intraoperative brain shifts. These brain shifts can be minimized with surgical technique improvements that are complementary to the proposed framework. For example, some studies reported that MRI-based STN targeting may eliminate the need for prolonged MER process, which can significantly reduce brain shifts caused by CSF egress [51] and can also reduce the risk of hemorrhagic complications in comparison with the overall 5.0 % hemorrhagic incidence in functional neurosurgery [52]. Alternately, the Interactive Brain Imaging System (IBIS) [53] prototype neuronavigation platform addresses surgical navigation issues related to brain shift via intraoperative freehand ultrasound measurements used to update patient-to-preoperative image alignment. We are currently integrating our trajectory planning algorithm to the IBIS platform. Thus, for surgical techniques requiring multiple MER penetrations, our automatic trajectory analysis could be executed before each penetration (in less then 20 s) using updated preoperative MRIs and could potentially assist the neurosurgeon toward his choice of lateral track for the next penetration.

Regarding the choice of implemented surgical constraints, our framework integrates common constraints found in other related work. The constraints found in Brunenberg et al.'s work [28] and Shamir et al. [29] are exactly covered by our constraints #1–5 although our technique is applied to denser SWI–TOF datasets. However, we added new constraints, for minimizing the overlap with the caudate and deep cortical gray matter, based on previous findings [33]. The work Essert et al.'s [10] also introduced geometric constraints to the trajectory length and orientation. These constraints are indirectly achieved by our framework with the restriction posed on the search space (constraints #1 and #2). However, no minimization of the path length occurs inside the allowed search space because a slightly longer but safer path is preferred to a shorter but riskier path. Furthermore, once inside the allowed search space, we decided not to pose further optimization to the electrode orientation because, as shown earlier in Fig. 1, we observed important variations in the choice of insertion angles across multiple subjects. Overall, the surgical constraints presented in this work were defined to minimize risks of surgical complications related to electrode insertion. With the increasing number of available contacts on new generations of lead models, DBS with multiple active contacts and multiple targets may yield new trajectory planning requirements to address stimulation-related complications preoperatively, before making the burr hole. For example, optimizing the lead orientation may become key for maximizing the overlap between the extracellular electric field and the shape of targeted structures while concurrently minimizing the spread of electric field into the internal capsule, the oculomotor nerve root and other white matter structures for prevention of stimulation side effects (e.g., muscle contraction, diplopia, etc.). These new requirements can be gradually incorporated into our generically designed path planning framework as they are discovered to interplay with the surgeon's decision-making.

During our experiments, we noted the neurosurgeon's interest in examining multiple insertion alternatives based on our computed trajectory ranking. This particular behavior could simply mean that an absolute optimal trajectory does not exist. Instead, many suitable trajectories may exist, each consisting of a trade-off among competing factors. With our set of implemented constraints, the recommended trajectories are typically distributed in multiple, well-delimited, patches of low-risk entry points rather than a single smooth patch with one local minimum. Thus, the surgeon can always examine the alternate low-risk trajectories, by jumping to a different insertion zone (e.g., in another gyrus that the surgeon is more comfortable with), in a timely matter using the visualization software presented in section "DBS planning framework".

We found it challenging to determine an optimal choice of weights for the different surgical constraints. The set of constraints and their optimal weighting may depend upon the surgeon and even the targeted nuclei. It could be interesting to investigate the concept of Pareto-optimality [54], used by Seitel et al. [55] for computer-assisted planning of radiofrequency ablation image-guided surgery. This principle yields computation of a Pareto-frontier map that encompasses all trajectories where there is no other trajectory that scores better for one constraint without scoring worse for any other constraint. As observed by Essert et al. [10], any trajectory optimized using a weight-based cost function will lie on the Pareto-frontier. Our software currently allows semi-automatic exploration of other Pareto-optimal points simply by changing the weights, which re-runs the constraint aggregation step and updates the color-coded map of recommended entry points in less then a second. Clearly, the Pareto-optimality principle can become a useful tool for studying different weighting patterns. For clinical use, it may be more intuitive to let the surgeon specify the relative importance of the surgical constraints and to recommend trajectories that were aggregated accordingly.

Overall, manual path planning, especially with dense multi-modal datasets, is a complex and lengthy process that yields subjective and possibly sub-optimal solutions. This work provides neurosurgeons with an intuitive tool that allows objective and patient-specific optimization of DBS lead trajectories, which may improve insertion safety and reduce surgical time. Although it is applied here to insertion of deep brain stimulation leads, the framework can be generalized to a wide variety of intracranial procedures, including trajectory planning for biopsies, endoscopy, insertion of depth electrodes and approach corridors to deep-seated tumors. Future work will concentrate on improving our SWI sequence to enhance the contrast between surface veins and CSF, and to improve their automatic segmentation. Furthermore, we will integrate our new framework with the overall surgical workflow for planning future DBS cases within the context of a prospective study.

Acknowledgments This research was funded by the Natural Sciences and Engineering Research Council of Canada (NSERC) and the Centres of Excellence for Commercialization and Research (CECR).

Conflict of interest None.

References

1. Kringelbach ML, Jenkinson N, Owen SL, Aziz TZ (2007) Translational principles of deep brain stimulation. Nat Rev Neurosci 8(8):623–635
2. de Lau LML, Breteler MMB (2006) Epidemiology of Parkinson's disease. Lancet Neurol 5(6):525–535

3. Baltuch GH, Stern MB (2007) Deep brain stimulation for Parkinson's disease, 1st edn. Informa healthcare, New York
4. Lind G, Schechtmann G, Lind C, Winter J, Meyerson BA, Linderoth B (2008) Subthalamic stimulation for essential tremor. Short- and long-term results and critical target area. Stereotact Funct Neurosurg 86(4):253–258
5. Duval C, Panisset M, Bertrand G, Sadikot AF (2000) Evidence that ventrolateral thalamotomy may eliminate the supraspinal component of both pathological and physiological tremors. Exp Brain Res 132(2):216–222
6. St-Jean P, Sadikot AF, Collins L, Clonda D, Kasrai R, Evans AC, Peters TM (1998) Automated atlas integration and interactive three-dimensional visualization tools for planning and guidance in functional neurosurgery. IEEE Trans Med Imaging 17(5):672–680
7. Sadikot AF, Chakravarty MM, Bertrand G, Rymar VV, Al-Subaie F, Collins DL (2011) Creation of computerized 3D MRI-integrated atlases of the human basal ganglia and thalamus. Front Syst Neurosci 5:71
8. Benabid AL, Chabardes S, Mitrofanis J, Pollak P (2009) Deep brain stimulation of the subthalamic nucleus for the treatment of Parkinson's disease. Lancet Neurol 8(1):67–81
9. Strafella AP, Vanderwerf Y, Sadikot AF (2004) Transcranial magnetic stimulation of the human motor cortex influences the neuronal activity of subthalamic nucleus. Eur J Neurosci 20(8): 2245–2249
10. Essert C, Haegelen C, Lalys F, Abadie A, Jannin P (2011) Automatic computation of electrode trajectories for deep brain stimulation: a hybrid symbolic and numerical approach. Int J Comput Assist Radiol Surg 1–16
11. Elolf E, Bockermann V, Gringel T, Knauth M, Dechent P, Helms G (2007) Improved visibility of the subthalamic nucleus on high-resolution stereotactic MR imaging by added susceptibility (T2*) contrast using multiple gradient echoes. Am J Neuroradiol 28(6):1093–1094
12. Xiao Y, Beriault S, Pike GB, Collins DL (2011) Multi-contrast multi-echo FLASH MRI for targeting the subthalamic nucleus. Magn Reson Imaging
13. D'Haese PF, Cetinkaya E, Konrad PE, Kao C, Dawant BM (2005) Computer-aided placement of deep brain stimulators: from planning to intraoperative guidance. IEEE Trans Med Imaging 24(11):1469–1478
14. Guo T, Parrent AG, Peters TM (2007) Automatic target and trajectory identification for deep brain stimulation (DBS) procedures. In: Ayache N, Ourselin S, Maeder A (eds) MICCAI 2007. LNCS, vol 4791, pp 483–490
15. McIntyre CC, Mori S, Sherman DL, Thakor NV, Vitek JL (2004) Electric field and stimulating influence generated by deep brain stimulation of the subthalamic nucleus. Clin Neurophysiol 115(3):589–595
16. Butson CR, Cooper SE, Henderson JM, McIntyre CC (2007) Patient-specific analysis of the volume of tissue activated during deep brain stimulation. Neuroimage 34(2):661–670
17. Nowinski WL, Yang GL, Yeo TT (2000) Computer-aided stereotactic functional neurosurgery enhanced by the use of the multiple brain atlas database. IEEE Trans Med Imaging 19(1):62–69
18. Lee JD, Huang CH, Lee ST (2002) Improving stereotactic surgery using 3-D reconstruction. IEEE Eng Med Biol Mag 21(6):109–116
19. Nowinski WL, Volkau I, Marchenko Y, Thirunavuukarasuu A, Ng TT, Runge VM (2009) A 3D model of human cerebrovasculature derived from 3 T magnetic resonance angiography. Neuroinformatics 7(1):23–36
20. Nowinski WL, Chua BC, Volkau I, Puspitasari F, Marchenko Y, Runge VM, Knopp MV (2010) Simulation and assessment of cerebrovascular damage in deep brain stimulation using a stereotactic atlas of vasculature and structure derived from multiple 3- and 7-tesla scans. J Neurosurg 113(6):1234–1241
21. Navkar N, Tsekos N, Stafford J, Weinberg J, Deng Z (2010) Visualization and planning of neurosurgical interventions with straight access. In: Navab N, Jannin P (eds) IPCAI 2010. LNCS, vol 6135, Springer, Heidelberg, pp 1–11
22. Graves MJ (1997) Magnetic resonance angiography. Br J Radiol 70:6–28
23. D'Haese PF, Pallavaram S, Li R, Remple MS, Kao C, Neimat JS, Konrad PE, Dawant BM (2012) CranialVault and its CRAVE tools: a clinical computer assistance system for deep brain stimulation (DBS) therapy. Med Image Anal 16(3):744–753
24. Vaillant M, Davatzikos C, Taylor R, Bryan R (1997) A path-planning algorithm for image-guided neurosurgery. In: Troccaz J, Grimson E, Mösges R (eds) CVRMed-MRCAS'97. LNCS, vol 1205, Springer, Heidelberg, pp 467–476
25. Fujii T, Asakura H, Emoto H, Sugou N, Mito T, Shibata I (2002) Automatic path searching for minimally invasive neurosurgical planning. Proc SPIE Med Imaging 4681:527–538
26. Tirelli P, De Momi E, Borghese NA, Ferrigno G (2009) An intelligent atlas-based planning system for keyhole neurosurgery. Int J Comput Assist Radiol Surg 4(suppl 1):S85–S91
27. Fujii T, Emoto H, Sugou N, Mito T, Shibata I (2003) Neuropath planner-automatic path searching for neurosurgery. International Congress Series, vol 1256, pp 587–596
28. Brunenberg E, Vilanova A, Visser-Vandewalle V, Temel Y, Ackermans L, Platel B, ter Haar Romeny B (2007) Automatic trajectory planning for deep brain stimulation: a feasibility study. In: Ayache N, Ourselin S, Maeder A (eds) MICCAI 2007. LNCS, vol 4791. Springer, Heidelberg, pp 584–592
29. Shamir R, Tamir I, Dabool E, Joskowicz L, Shoshan Y (2010) A method for planning safe trajectories in image-guided keyhole neurosurgery. In: Jiang T, Navab N, Pluim J, Viergever M (eds) MICCAI 2010. LNCS, vol 6363. Springer, Heidelberg, pp 457–464
30. Danielsson P-E (1980) Euclidean distance mapping. Comput Graph Image Process 14:227–248
31. Haacke EM, Mittal S, Wu Z, Neelavalli J, Cheng YC (2009) Susceptibility-weighted imaging: technical aspects and clinical applications, part 1. AJNR Am J Neuroradiol 30(1):19–30
32. Haacke EM, Xu Y, Cheng YC, Reichenbach JR (2004) Susceptibility weighted imaging (SWI). Magn Reson Med 52(3):612–618
33. Beriault S, Al Subaie F, Mok K, Sadikot AF, Pike GB (2011) Automatic trajectory planning of DBS neurosurgery from multi-modal MRI datasets. In: Fichtinger G, Martel AL, Peters TM (eds) MICCAI 2011. LNCS, vol 6891. Springer, Heidelberg, pp 259–266
34. Zrinzo L, van Hulzen AL, Gorgulho AA, Limousin P, Staal MJ, De Salles AA, Hariz MI (2009) Avoiding the ventricle: a simple step to improve accuracy of anatomical targeting during deep brain stimulation. J Neurosurg 110(6):1283–1290
35. Elias WJ, Sansur CA, Frysinger RC (2009) Sulcal and ventricular trajectories in stereotactic surgery. J Neurosurg 110(2):201–207
36. Sadowski EA, Bennett LK, Chan MR, Wentland AL, Garrett AL, Garrett RW, Djamali A (2007) Nephrogenic systemic fibrosis: risk factors and incidence estimation. Radiology 243(1):148–157
37. Sled JG, Zijdenbos AP, Evans AC (1998) A nonparametric method for automatic correction of intensity nonuniformity in MRI data. IEEE Trans Med Imaging 17(1):87–97
38. Nyul LG, Udupa JK, Xuan Z (2000) New variants of a method of MRI scale standardization. IEEE Trans Med Imaging 19(2):143–150
39. Smith SM (2002) Fast robust automated brain extraction. Hum Brain Mapp 17(3):143–155
40. Smith SM, Jenkinson M, Woolrich MW, Beckmann CF, Behrens TE, Johansen-Berg H, Bannister PR, De Luca M, Drobnjak I, Flitney DE, Niazy RK, Saunders J, Vickers J, Zhang Y,

De Stefano N, Brady JM, Matthews PM (2004) Advances in functional and structural MR image analysis and implementation as FSL. Neuroimage 23(suppl 1):S208–S219

41. Fonov V, Evans AC, Botteron K, Almli CR, McKinstry RC, Collins DL (2011) Unbiased average age-appropriate atlases for pediatric studies. Neuroimage 54(1):313–327
42. Collins DL, Neelin P, Peters TM, Evans AC (1994) Automatic 3D intersubject registration of MR volumetric data in standardized Talairach space. J Comput Assist Tomogr 18(2):192–205
43. Collins DL, Holmes C, Peters T, Evans A (1995) Automatic 3D model-based neuroanatomical segmentation. Hum Brain Mapp 3:190–208
44. Collins L, Zijdenbos A, Baare W, Evans A (1999) ANIMAL+INSECT: improved cortical structure segmentation. In: Kuba A, Šáamal M, Todd-Pokropek A (eds) IPMI 1999. LNCS. Springer, Heidelberg, pp 210–223
45. Coupe P, Manjon JV, Fonov V, Pruessner J, Robles M, Collins DL (2011) Patch-based segmentation using expert priors: application to hippocampus and ventricle segmentation. Neuroimage 54(2):940–954
46. Frangi A, Niessen W, Vincken K, Viergever M (1998) Multiscale vessel enhancement filtering. In: Wells WM, Colchester ACF, Delp SL (eds) MICCAI 1998. LNCS, vol 1496. Springer, Heidelberg, pp 130–137
47. Essert C, Haegelen C, Jannin P (2010) Automatic computation of electrodes trajectory for deep brain stimulation. In: Liao H, Edwards P, Pan X, Fan Y, Yang G-Z (eds) MIAR 2010. LNCS, vol 6326. Springer, Heidelberg, pp 149–158
48. Yoo TS, Ackerman MJ, Lorensen WE, Schroeder W, Chalana V, Aylward S, Metaxas D, Whitaker R (2002) Engineering and algorithm design for an image processing API: a technical report on ITK—the insight toolkit. Stud Health Technol Inf 85:586–592
49. Schroeder W, Martin K, Lorensen B (2002) The visualization toolkit, 3rd edn
50. Xu Y, Haacke EM (2006) The role of voxel aspect ratio in determining apparent vascular phase behavior in susceptibility weighted imaging. Magn Reson Imaging 24(2):155–160
51. Petersen EA, Holl EM, Martinez-Torres I, Foltynie T, Limousin P, Hariz MI, Zrinzo L (2010) Minimizing brain shift in stereotactic functional neurosurgery. Neurosurgery 67(3 suppl operative):ons213–ons221
52. Zrinzo L, Foltynie T, Limousin P, Hariz MI (2012) Reducing hemorrhagic complications in functional neurosurgery: a large case series and systematic literature review. J Neurosurg 116(1):84–94
53. Mercier L, Del Maestro RF, Petrecca K, Kochanowska A, Drouin S, Yan CX, Janke AL, Chen SJ, Collins DL (2011) New prototype neuronavigation system based on preoperative imaging and intraoperative freehand ultrasound: system description and validation. Int J Comput Assist Radiol Surg 6(4):507–522
54. Mathur VK (1991) How well do we know Pareto optimality? J Econ Educ 22(2):172–178
55. Seitel A, Engel M, Sommer CM, Radeleff BA, Essert-Villard C, Baegert C, Fangerau M, Fritzsche KH, Yung K, Meinzer HP, Maier-Hein L (2011) Computer-assisted trajectory planning for percutaneous needle insertions. Med Phys 38(6):3246–3259